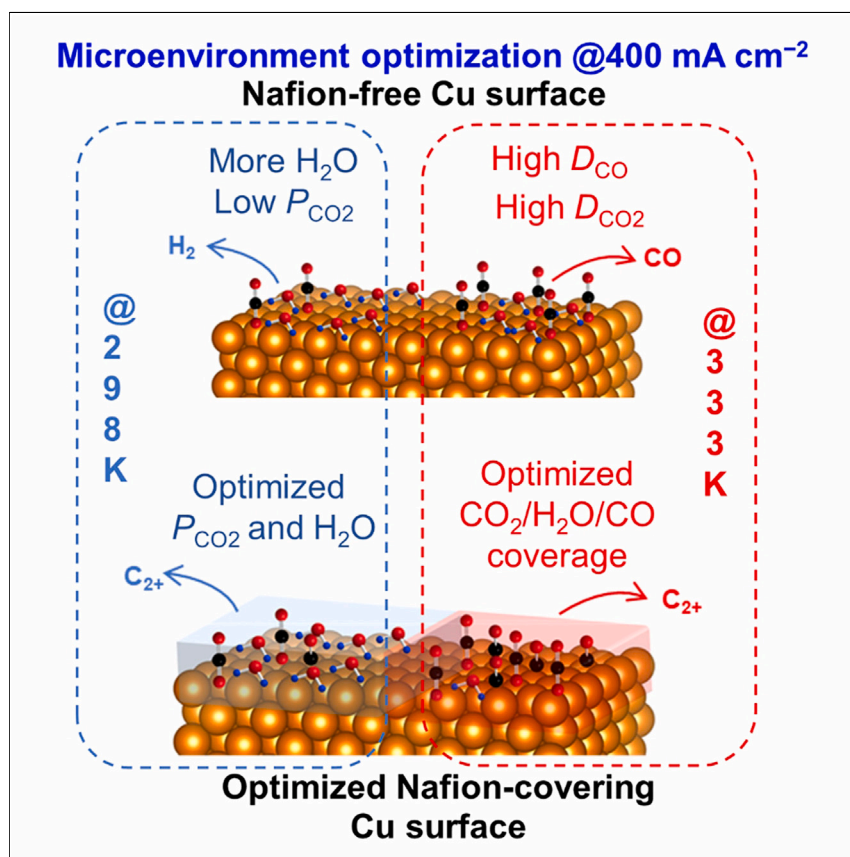


## Article

# Selectivity control by modifying pressure, temperature, and ionomer decoration for CO<sub>2</sub> electroreduction using gas-diffusion Cu electrodes



Product distribution control over Cu was achieved during CO<sub>2</sub> electroreduction by changing the “beyond catalyst” factors, including operating pressure, temperature, and ionomer decoration, under industrially relevant conditions.

Xiaofei Lu, Tengisbold Gankhuyag, Keisuke Obata, Yuhang Yu, Kazuhiro Takanabe  
takanabe@chemsys.t.u-tokyo.ac.jp

### Highlights

“Beyond catalyst” factors were examined at industrially relevant current densities

Local microenvironment significantly changed the product distribution

Distinctive performances of Cu under different conditions were interpreted



Lu et al., Chem Catalysis 4, 101030  
July 18, 2024 © 2024 The Author(s). Published by Elsevier Inc.  
<https://doi.org/10.1016/j.cheecat.2024.101030>



## Article

Selectivity control by modifying pressure, temperature, and ionomer decoration for CO<sub>2</sub> electroreduction using gas-diffusion Cu electrodesXiaofei Lu,<sup>1</sup> Tengisbold Gankhuyag,<sup>1</sup> Keisuke Obata,<sup>1</sup> Yuhang Yu,<sup>1</sup> and Kazuhiro Takanahe<sup>1,2,\*</sup>

## SUMMARY

“Beyond catalyst” factors influencing the performance of Cu-based CO<sub>2</sub> electroreduction were investigated based on rigorous microkinetic analysis under industrially relevant conditions. Our experimental results indicated that the activity and selectivity of Cu-based CO<sub>2</sub> electroreduction were not unaffected by electrolyte pH changes but were significantly influenced by operating conditions including pressure and temperature. Analyzing the kinetic data concerning CO<sub>2</sub> partial pressure ( $P_{\text{CO}_2}$ ) and operating temperature revealed that higher  $P_{\text{CO}_2}$  ( $\geq 25$  kPa) or higher reaction temperature ( $\leq 333$  K) favored CO formation, coinciding with a reduction of the C<sub>2+</sub> and formate pathways. Product distribution control at 333 K was achieved by engineering the structure of the Cu gas-diffusion electrode (GDE), where CO was exclusively produced on bare Cu, and the faradic efficiency of C<sub>2+</sub> was enhanced by introducing an optimized Nafion ionomer content in the catalyst layer, likely ascribable to the modulation of diffusion coefficients of reactants (e.g., CO<sub>2</sub> and H<sub>2</sub>O) and key intermediates (e.g., CO).

## INTRODUCTION

Electrochemical CO<sub>2</sub> reduction powered by renewable electricity holds great promise for addressing the challenges of CO<sub>2</sub> emissions and achieving a sustainable future.<sup>1,2</sup> Accordingly, significant advancements, including state-of-the-art electrocatalysts and next-generation electrolyzers, have been achieved in the past decades, demonstrating the potential of producing fossil-free fuels and chemicals.<sup>3–7</sup> Nevertheless, related techno-economic analyses have emphasized the need to reduce the power inputs in both CO<sub>2</sub> electrolyzers and their corresponding downstream separations.<sup>8</sup> For example, improvements in the faradic efficiency (FE) of ethylene (C<sub>2</sub>H<sub>4</sub>) from 47% to 57% can result in a 25% reduction in heating input during downstream separation.<sup>9</sup> More specifically, achieving 50% full-cell energy efficiency (EE) and FE of CO<sub>2</sub> reduction >80% at commercially relevant conditions (e.g., >200 mA cm<sup>-2</sup> and >1,000 h durability)—competitive with conventional chemical processes—is generally considered the goal.<sup>8–10</sup> In this context, most reported electrolyzers (e.g., EE < 40% at 200 mA cm<sup>-2</sup> and <50 h stability) still cannot fulfill the requirement, highlighting the need for the advancement of electrocatalysts that are both active and selective, along with the development of sophisticated system designs suitable for large-scale implementation.

Several electrocatalysts (e.g., Au, Ag, and molecular complexes) have been demonstrated to catalyze CO<sub>2</sub> toward single-carbon products (e.g., CO and formic acid) at nearly 100% selectivity, while it remains challenging to selectively produce multi-carbon

## THE BIGGER PICTURE

Electrocatalytically converting CO<sub>2</sub> into value-added and energy-dense chemicals stands out as a route for achieving a decarbonized society, particularly when driven by the electric power generated from renewable energy sources. However, the “beyond catalyst” phenomenon is often neglected in electrochemical CO<sub>2</sub> reduction, but it can significantly affect the performance of CO<sub>2</sub> electroreduction under industrially relevant conditions. In this context, a comprehensive understanding of all beyond catalyst factors over Cu-based gas-diffusion electrodes (GDEs) compatible with high current densities is provided, which includes feeding pressure, operating temperature, and ionomer decoration. These findings demonstrate the possibility of establishing general and convenient strategies by tuning beyond catalyst factors with a GDE-based electrolyzer to selectively generate specific products and improve economic viability.



products ( $C_{2+}$ ).<sup>6,7,11–13</sup> Currently, most studies are focused on the rational design of Cu-based electrocatalysts (e.g., facet, grain boundary, and compositions) to facilitate the formation of  $C_{2+}$  products.<sup>6</sup> However, the catalytic performance actually depends on the combined effects of material and reaction environment rather than those of the catalyst's structure and morphology alone.<sup>10,14,15</sup> It has been reported that the local reaction environment during  $CO_2$  reduction significantly affects the catalytic performance of copper-based electrocatalysts.<sup>10,14–16</sup> For example, the as-obtained current density of immersed electrodes in aqueous electrolytes is nearly two orders of magnitude lower than that using gas-diffusion electrodes (GDEs) at fixed overpotentials.<sup>10,15</sup> Previous studies have also reported that functionalized Cu with a molecular modifier could perturb the product selectivity of metallic Cu via the different degrees of diffusion of  $CO_2$  and  $H_2O$  to the surface.<sup>16</sup> A final extremely important parameter is reaction rate, which can also change the reaction microenvironment, such as local pH and local  $CO_2$  concentration. For instance, electrolytes with different buffering capacities could establish different local pH gradients at the electrode-electrolyte interface, significantly influencing product distributions by affecting the competing reactions.<sup>10,17,18</sup> Therefore, without considering the varied reaction microenvironment, there is a potential risk of optimizing the surface properties of electrocatalysts in an inadequate manner. As a consequence of these, the in-depth reaction condition investigation assessed at commercially relevant conditions rather than at substantially lower current densities is becoming increasingly essential in the rational design of electrocatalysts and reactor configurations.

In addition to catalyst development, increasing operating temperature has also been demonstrated as a successful approach to reducing overvoltage for some practical electrochemical processes (e.g., fuel cells and water electrolyzers) resulting from the increased reaction kinetics and reduced ohmic potential loss.<sup>19,20</sup> Studying the temperature-dependent performance of  $CO_2$  reduction is of growing importance to meet its practical application. Zhuang and co-workers<sup>21</sup> revealed that the cell voltage of CO evolution over polycrystalline (PC) Au decreased from 2.5 to 2.2 V when the operating temperature was increased from 303 to 353 K using a membrane electrode assembly (MEA) electrolyzer, mainly due to the enhanced kinetics of anodic and cathodic reactions. It should be noted that the  $FE_{CO}$  declined from 96% at 303 K to 72% at 353 K because the hydrogen ( $H_2$ ) evolution reaction (HER) was also facilitated on the PC Au electrode used at elevated temperatures.<sup>21</sup> Löwe et al. reported that the optimized operation temperature on a tin-oxide-loaded GDE in electrocatalytic  $CO_2$  reduction toward formate ( $HCOO^-$ ) was 323 K when considering the opposing influence of temperature on the  $CO_2$  diffusion coefficient and solubility near the electrode surface.<sup>22</sup> The temperature performance over PC Cu in aqueous solutions disclosed that lower temperature (273–275 K) favored  $CH_4$  formation (ca. 50%) at the expense of  $C_2H_4$  (only 10%), and the HER dominated the surface reaction at increased temperature, likely arising from the reduced  $CO_2$  solubility.<sup>23–25</sup> It is noteworthy that this examination was performed at substantially lower current densities (5–10  $mA\ cm^{-2}$ ). Notwithstanding these obtained advancements, the complexities of temperature-dependent performance on Cu are far from being completely understood. A systematic investigation is necessary to assess the impact of temperature on the product distribution at commercially relevant current densities, which can be used for system optimization.

Although previous studies have already pointed out the importance of electrolytes and reaction temperature on the catalytic performance of Cu during electrocatalytic  $CO_2$  reduction, they were mostly performed at substantially lower current densities and not at industrially relevant current densities using GDEs. We systematically examined

<sup>1</sup>Department of Chemical System Engineering, The University of Tokyo, School of Engineering, 7-3-1 Hongo, Bunkyo-ku, Tokyo 113-8656, Japan

<sup>2</sup>Lead contact

\*Correspondence:  
takanabe@chemsys.t.u-tokyo.ac.jp  
<https://doi.org/10.1016/j.checat.2024.101030>

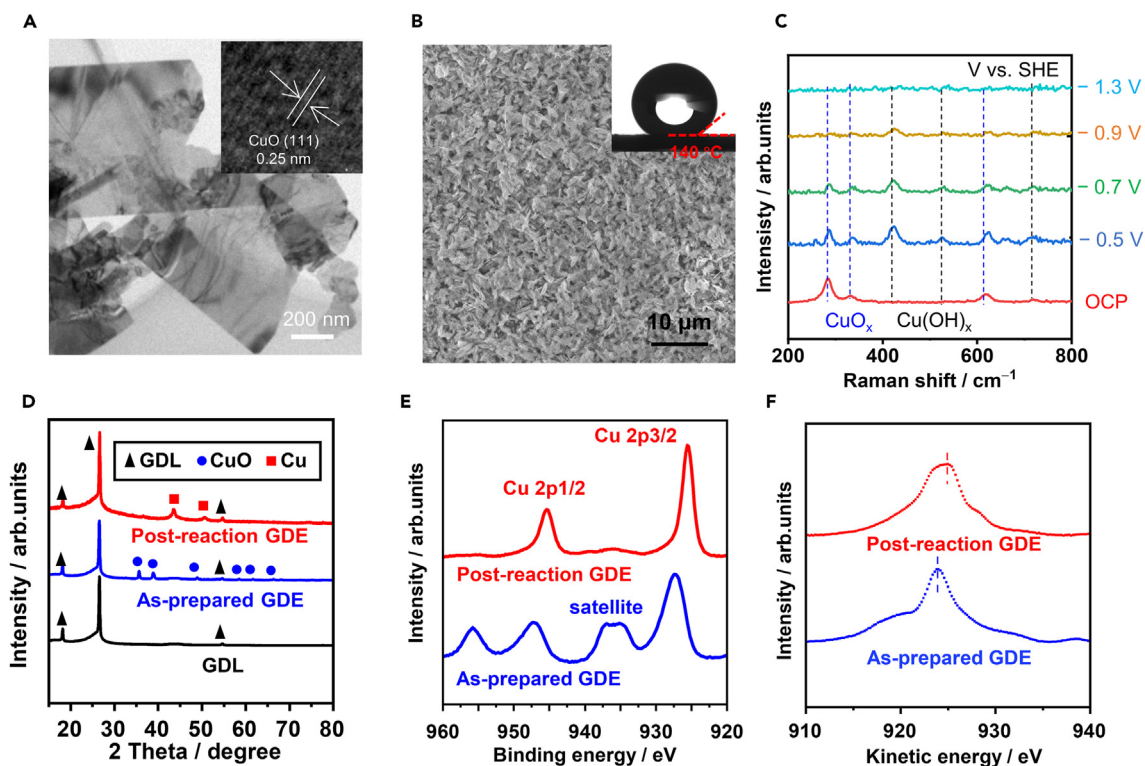


**Figure 1. Characterization of the working electrode**

(A) TEM images of the as-synthesized Cu composite.

(B) SEM image of the as-prepared Cu gas-diffusion electrode (GDE) and inset image show the water contact angle at around 140°.

(C) *In situ* Raman spectroscopy monitoring the pre-reduction processes at various applied potentials in 1 M KHCO<sub>3</sub> at 298 K. SHE means standard hydrogen electrode.

(D) X-ray diffraction patterns of pristine Cu GDE and Cu GDE after reduction together with bare gas-diffusion layer (GDL).

(E) XPS analysis of Cu 2p regions of the pristine Cu GDE and Cu GDE after reduction.

(F) Auger emission spectra of Cu LMM region of the pristine Cu GDE and Cu GDE after reduction.

the prominent “beyond catalyst” factors affecting the performance of CO<sub>2</sub> electroreduction over Cu GDEs at industrially relevant current densities. Using high-surface-area Cu as the model catalyst, rigorous microkinetic analysis was carried out, including electrolyte effects, Tafel analysis, and pressure/temperature-dependent results. We found that the performance of the as-obtained Cu GDE was significantly affected by the partial pressure of CO<sub>2</sub> ( $P_{\text{CO}_2}$ ) and operating temperature. Interestingly, at elevated temperatures, the reaction pathway can be selectively directed toward CO or C<sub>2+</sub> formation by engineering the electrode structure. Gaining insights into the impact of these factors on electrochemical CO<sub>2</sub> reduction and utilizing these dependencies to design advanced systems are crucial for enhancing the performance of cutting-edge electrocatalysts.

## RESULTS

### Synthesis and characterization of Cu-based electrocatalysts

Cu is currently the most effective material for producing valuable C<sub>2+</sub> products.<sup>6</sup> We, therefore, started with the synthesis of a Cu composite via a hydrothermal method (see the [supplemental information](#)). The morphology of the catalyst was characterized by scanning electron microscopy (SEM) and transmission electron microscopy (TEM) to be micrometer-sized flakes (Figures 1A and S1A). The X-ray diffraction (XRD) pattern of the as-synthesized composite in Figure S1B exhibited characteristic peaks compatible with CuO, in good agreement with high-resolution TEM results (interplanar spacing of

0.25 nm for the CuO (111) facet in the inset of Figure 1A). The working electrodes, referred to as Cu GDEs, were prepared by airbrushing an ink containing a mixture of CuO and Nafion ionomer on a C-based gas-diffusion layer (GDL). As shown in the SEM image (Figure 1B), the Cu composite was uniformly coated on the GDL with a porous, three-dimensional structure (ca. 2  $\mu\text{m}$  thickness) (Figure S2), and the corresponding loading was around 0.5–0.7  $\text{mg cm}^{-2}$ . The hydrophobicity of the catalytic layer with a water contact angle of around  $140^\circ$  (inset in Figure 1B) has proven decisive in maintaining sufficient gas transport toward the catalytically active sites by preventing electrolyte flooding. To disclose the oxidation state of Cu under reaction conditions, *in situ* Raman spectroscopy was performed to monitor the pre-reduction process, as shown in Figure 1C. Pristine CuO under open-circuit potential (OCP) showed the characteristic Raman peaks at 282, 330, and  $616\text{ cm}^{-1}$ , respectively.<sup>26</sup> Upon the application of a potential of  $-0.5\text{ V}$  with reference to a standard  $\text{H}_2$  electrode (SHE), several sharp peaks at approximately  $412$  and  $542\text{ cm}^{-1}$  appeared, accompanied by a reduction in the peak intensity observed at  $282\text{ nm}$ . This change was attributed to the reduction of copper oxide from Cu(II) to Cu(I), as indicated in prior studies.<sup>27</sup> Some peaks persisted at increasing cathodic potentials until  $-1.3\text{ V}_{\text{SHE}}$ , indicating the presence of oxides even at reaction conditions. Figure S3 displays a representative SEM image of reduced Cu, and the flake-like morphology was well maintained. In addition, Figure 1D exhibits the XRD patterns of the Cu GDE after reduction, along with CuO loaded on GDL and bare GDL for reference. The characteristic peaks observed at  $43.3^\circ$  and  $50.4^\circ$  correspond to metallic Cu. No extra characteristic peaks were obtained from the patterns, indicating that the amount of oxide species was very limited or they were amorphous.

The chemical state of the electrodes was further investigated by X-ray photoelectron spectroscopy (XPS) and Auger emission (AE) spectra of the Cu L-inner level-M-inner level-M-inner level electron transition (LMM) region, as shown in Figures 1E and 1F. The XPS peaks of as-prepared GDE located at  $954.2$  and  $934.2\text{ eV}$  in Figure 1E were ascribable to the oxidation states of Cu(II)  $2p_{1/2}$  and Cu(II)  $2p_{3/2}$ , respectively. After pre-reduction, two peaks of Cu shifted to lower electron-binding energies at ca.  $933.1$  and  $953.2\text{ eV}$ , compatible with the reductive-state Cu. The strong satellites from CuO almost disappeared, indicating that there was no apparent contribution originating from oxides, which is in good agreement with *in situ* Raman and XRD results. Consistently, the characteristic peaks of Cu(II) that appeared at  $918\text{ eV}$  in the Cu LMM region moved to a higher kinetic energy, approximately  $919\text{ eV}$ , attributable to the reductive state of Cu. All things considered, these observations indicated that the authentically catalytic sites were formed of metallic Cu under reaction conditions, although the presence of a tiny amount of oxidized Cu decorating the surface cannot be excluded.

Next, the  $\text{CO}_2$  electroreduction product distribution was assessed through chronopotentiometry (CP) measurements over a 30-min duration at different current densities ( $j$ ) in a gas-fed flow cell with an electrolyte of  $1\text{ M KHCO}_3$  at  $298\text{ K}$  and  $101\text{ kPa CO}_2$ . At each current density, a fresh electrode was used. The outlet gas products were analyzed using a gas chromatograph (GC), and the liquid products in the catholyte were quantified by nuclear magnetic resonance (NMR), where the major quantified products included  $\text{H}_2$ ,  $\text{CO}$ ,  $\text{C}_2\text{H}_4$ , ethanol ( $\text{C}_2\text{H}_5\text{OH}$ ), n-propanol (n-PrOH), and  $\text{HCOO}^-$ . The mass loadings of CuO were optimized to maximize the  $\text{C}_{2+}$  products and minimize  $\text{H}_2$  evolution occurring on the as-prepared Cu GDE (Figure S4). At low mass loadings (e.g.,  $0.2\text{ mg cm}^{-2}$ ),  $\text{H}_2$  evolution would dominate the surface reaction, and some  $\text{CH}_4$  would be formed at higher total current densities with higher overpotentials. With increasing of the mass loading, the

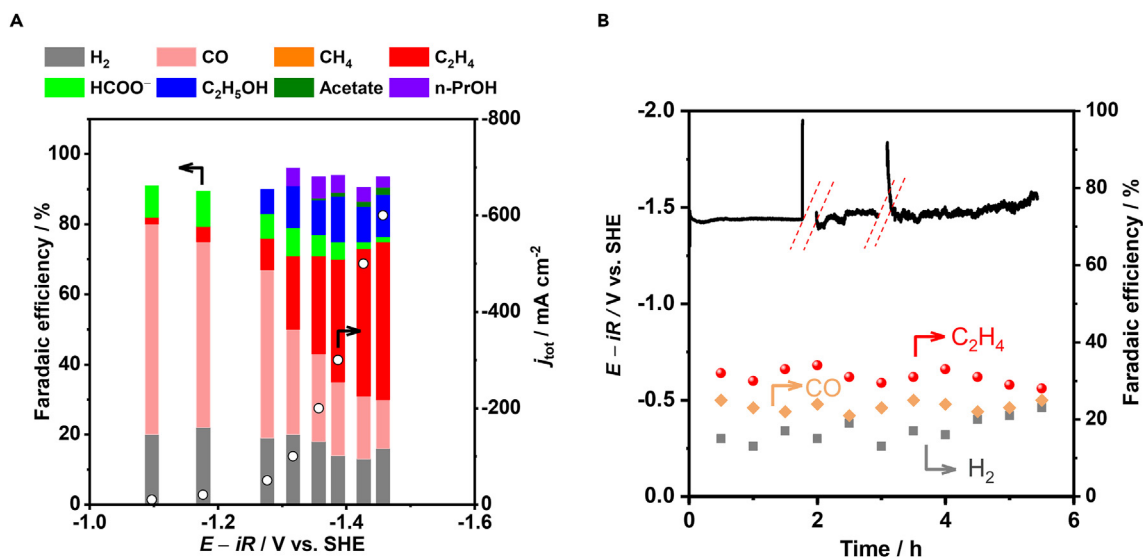


**Figure 2. Electrocatalytic CO<sub>2</sub> reduction reaction over the as-prepared GDE in a gas-fed flow cell**

(A) The total current density and cumulative faradaic efficiencies were recorded as a function of the applied potential, which was examined by 30-min chronopotentiometry measurement. n-PrOH means n-propanol

(B) Stability evaluation conducted at a current density of  $-200 \text{ mA cm}^{-2}$  for more than 5 h of electrolysis. Conditions: 1 M KHCO<sub>3</sub> electrolyte at 298 K and 101 kPa CO<sub>2</sub>.

product of CO<sub>2</sub> reduction, especially for C<sub>2+</sub>, was increased with lower overpotentials, and H<sub>2</sub> and CH<sub>4</sub> were suppressed simultaneously. There was an optimized value of ca. 0.8 mg cm<sup>-2</sup>, which will be used unless otherwise noted. Figure 2A summarizes the current densities and corresponding product distributions over the as-prepared GDE of Cu with respect to the applied potentials.  $j_{\text{tot}}$  increased exponentially at more cathodic potentials but with varied FEs. Interestingly, the H<sub>2</sub> evolution was always suppressed below 20%, and no CH<sub>4</sub> was detected across the whole potential range, likely resulting from the construction of gas-electrode-electrolyte interfaces, where sufficient CO<sub>2</sub> was allowed to be supplied to the catalyst surface. For gas products, the as-prepared Cu GDE preferred CO evolution at lower overpotentials, and FE<sub>CO</sub> significantly decreased with increasing overpotentials from ca. 60% at  $-1.1 \text{ V}_{\text{SHE}}$  to 15% at  $-1.46 \text{ V}_{\text{SHE}}$ . It produced a trace amount of C<sub>2</sub>H<sub>4</sub> at  $-1.1 \text{ V}_{\text{SHE}}$ , and FE<sub>C<sub>2</sub>H<sub>4</sub></sub> gradually elevated at more cathodic potentials, reaching close to 46% at  $-1.46 \text{ V}_{\text{SHE}}$ . Regarding the liquid products, only HCOO<sup>-</sup> was detected at  $j_{\text{tot}} < 20 \text{ mA cm}^{-2}$ . It should be noted that the too-small concentrations of liquid C<sub>2+</sub> products below the detection limitation of NMR likely resulted in the total FE < 100%. In more detail, potential-dependent FE was also observed for HCOO<sup>-</sup> and acetate. When FE<sub>HCOO<sup>-</sup></sub> was ca. 10% at  $-1.1 \text{ V}_{\text{SHE}}$ , FE<sub>HCOO<sup>-</sup></sub> decreased to <2% at  $-1.46 \text{ V}_{\text{SHE}}$ . In contrast, the FE of acetate was zero at  $> -1.36 \text{ V}_{\text{SHE}}$  initially but increased to ca. 2% at  $-1.46 \text{ V}_{\text{SHE}}$ , possibly attributable to the increased local pH at high reaction rates. Apart from the products mentioned above, FE<sub>C<sub>2</sub>H<sub>5</sub>OH</sub> and FE<sub>n-PrOH</sub> were almost independent of the applied potentials and stayed at approximately 10% and 4%, respectively. Clearly, the C<sub>2+</sub> formation rate is facilitated at the expense of C<sub>1</sub> formation (especially CO) through a C–C coupling reaction at high overpotentials, where the  $j_{\text{C<sub>2+ of around  $-400 \text{ mA cm}^{-2}$  was achieved at  $-1.46 \text{ V}_{\text{SHE}}$ . Interestingly, when normalized to the similar electrochemical surface area (ECSA), commercial CuO under identical conditions afforded activity comparable to that of as-prepared CuO GDE (Figure S5). Note that some small differences in product distributions likely originated from the different morphologies (e.g., void fraction) or surface structures (e.g., facet, grain boundary). These findings indicated</sub>$

that the intrinsic catalytic activity between as-prepared CuO and commercial CuO was identical at various electrode potentials.

In addition, the stability of as-prepared GDE was also examined by applying a constant current density of  $-200 \text{ mA cm}^{-2}$ , as plotted in Figure 2B. The findings demonstrated a consistent potential profile over a period of 5 h with no notable voltage fluctuations. The product distributions were almost identical throughout 5 h of electrolysis. The corresponding overpotential gradually increased, and  $\text{FE}_{\text{H}_2}$  increased after 5 h, probably because the hydrophobicity loss of GDE occurred and flooding was observed. In the broader context, durability plays a pivotal role in conducting accurate kinetic analysis, which is essential for understanding the influence of reaction conditions on electrochemical  $\text{CO}_2$  reduction at industrially significant current densities, as discussed in the following sections.

### Investigation of reaction pathways by electrokinetic measurements

Previous studies have commented on the importance of electrolytes during  $\text{CO}_2$  electrocatalysis, including ion identity, buffer capacity, and pH.<sup>28–34</sup> It is commonly accepted that cations can facilitate surface-mediated  $\text{CO}_2$  reduction via cation-non-covalent interactions by modifying the interfacial electric field.<sup>29,30,34</sup> However, conflicting conclusions of anion effect have been reported, likely resulting from the varied local reaction environment, which complicated efforts to design a suitable electrocatalytic system.<sup>35–37</sup> Herein, four different electrolytes with varied bulk pH and buffer capacity, including 0.5 M  $\text{K}_2\text{SO}_4$  (pH 7), 1 M K-phosphate (pH 7.2), 1 M  $\text{KHCO}_3$  (pH 8.3), and 1 M KOH (pH 13.5), were utilized to examine the influences of pH and buffer capacity on electrochemical  $\text{CO}_2$  reduction using a Cu GDE. The current density range between 20 and  $300 \text{ mA cm}^{-2}$  was selected to meet the industrial requirement.

Figure 3A provides the potential dependencies of  $j_{\text{C-based products}}$  at  $P_{\text{CO}_2} = 101 \text{ kPa}$  and 298 K in different electrolytes.  $j_{\text{C-based products}}$  was observed to be almost unaffected by changes in pH and buffer capacity (constant behavior in the SHE scale). These results suggested that the rate-determining step (RDS) did not involve  $\text{H}^+$  and  $\text{OH}^-$ . Unlike the irrelevant  $j_{\text{C-based products}}$ ,  $j_{\text{H}_2}$  in 1 M K-phosphate was clearly higher than that in other electrolytes (Figure 3D). This difference is due to the ability of buffering capacity to affect the local pH associated with concentration and buffer pKa, namely electrolyte engineering.<sup>38</sup> To quantitatively describe the local reaction conditions, we calculated the local pH for each tested electrolyte as a function of current density by building a diffusion-reaction model similar to the works of the Bell group and the Jiao group (see supplemental information for further details).<sup>17,35</sup> In all electrolytes, the surface pH increased with increased reaction rate (Figure 3B). It should be noted that the neutralization reaction between KOH and  $\text{CO}_2$  was considered under reaction conditions, leading to the shifted pH of KOH typed electrolyte from 13.5 to ca. 12.5. As expected, the local pH on the electrode surface in unbuffered 0.5 M  $\text{K}_2\text{SO}_4$  (pH 7) was dramatically higher than the bulk pH under all investigated current densities due to the generation of  $\text{OH}^-$  without replenishment by buffer species. In contrast, 1.0 M K-phosphate (pH 7.2, close to phosphate pKa) resulted in a slight increase compared to the bulk pH due to the strong buffer capacity of phosphate. KOH (1.0 M) neutralized with  $\text{CO}_2$  (pH  $\sim 12.5$ ) is alkaline enough to have sufficient  $\text{OH}^-$ , and  $\text{KHCO}_3$  (pH 8.3) approaches its pKa of  $\sim 10.5$ . So, the different local pH in different electrolytes triggers the switching of the reactants for  $\text{H}_2$  evolution from free  $\text{H}_3\text{O}^+$ , HA (where A represents a buffer anion), and  $\text{H}_2\text{O}$  (more difficult to react in this order),<sup>38</sup> which well explains the obtained trend of  $j_{\text{H}_2}$ . Furthermore, the ratios between  $j_{\text{C}2+}$  and  $j_{\text{C}1}$  were also plotted with respect to

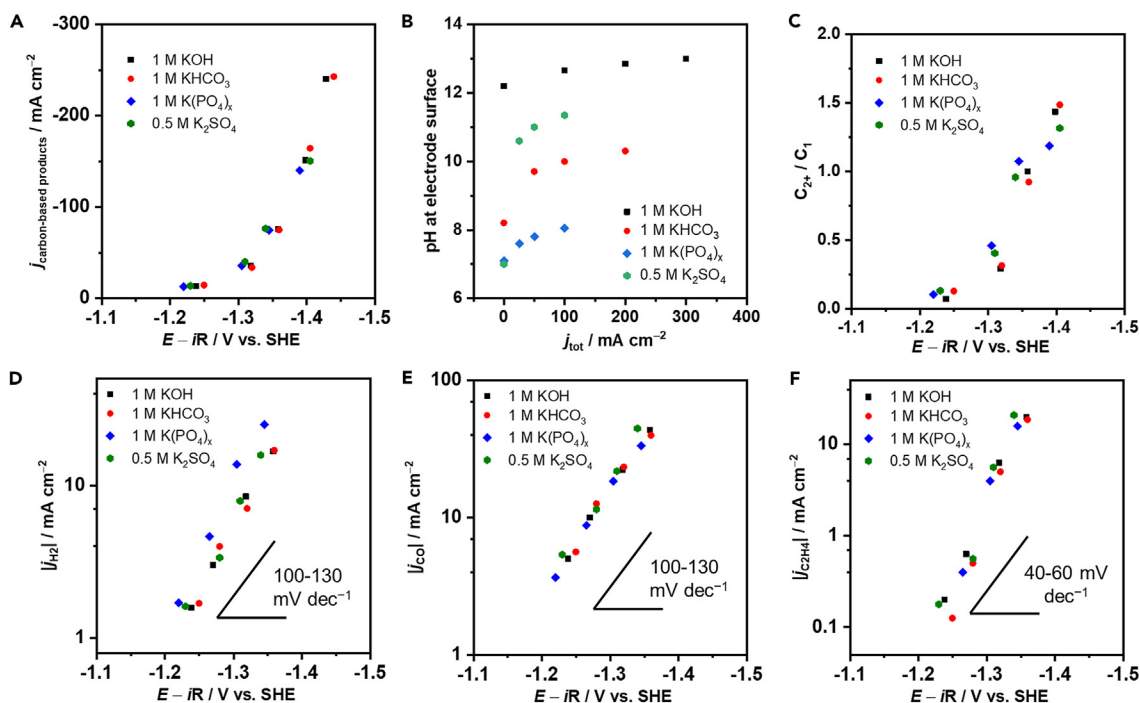


**Figure 3. Electrokinetic data for electrochemical CO<sub>2</sub> reduction**

- (A) Total current density of C-based products in relation to the applied potential in various electrolytes.  
(B) The calculated local pH with respect to the total current densities in various electrolytes.  
(C) The ratios of C<sub>2+</sub> products versus C<sub>1</sub> products for different electrolytes.  
(D) The kinetic current densities of H<sub>2</sub> are summarized in various electrolytes dependent on electrode potential.  
(E) The kinetic current densities of CO are summarized in various electrolytes dependent on electrode potential.  
(F) The kinetic current densities of C<sub>2</sub>H<sub>4</sub> are summarized in various electrolytes dependent on electrode potential.

the applied potentials in Figure 3C, which predominantly overlapped in various electrolytes. There does not appear to be any strong correlations between electrolytes (anion identity, pH, and buffering capacity) and carbon-based product distribution (not including methane). These findings were different from the previous reports on Cu-based electrocatalysts for CO<sub>2</sub> reduction, where the enhanced C<sub>2+</sub> formation rate under higher pH was observed,<sup>36,37,39</sup> likely resulting from the varied local reaction environments in different studies or different experimental designs.

Analyzing the current-potential relationship was used to clarify the RDS of the CO<sub>2</sub> electroreduction over Cu. Figures 3D–3F display the relationship between current density and applied potential as a form of the Tafel plots for the products, including H<sub>2</sub>, CO, and C<sub>2</sub>H<sub>4</sub>, respectively, in a wide pH range from 7 to 14 on the SHE scale. For H<sub>2</sub> evolution (as a benchmark of Tafel slope analysis), an unchanging Tafel slope value of around 120 mV dec<sup>-1</sup> was detected in all cases (Figure 3D), consistent with that obtained in previous studies, where the Volmer step was reported as the RDS in the H<sub>2</sub> evolution on Cu. This quantity also indicated that there is no mass transport limitation of the proton source in our system, which holds great importance for accurately conducting Tafel slope analysis for CO<sub>2</sub> electroreduction. Tafel slopes, however, reflect the information about RDS only, so that Tafel analysis using the partial current density of the products that are formed after the common RDS gives little physical insight to indicate the reaction mechanism (ca. 120 for CO [Figure 3E] and <60 mV dec<sup>-1</sup> for C<sub>2</sub>H<sub>4</sub> [Figure 3F] during CO<sub>2</sub> electroreduction). Nevertheless, independent Tafel slope values among different electrolytes for CO and C<sub>2</sub>H<sub>4</sub> formation are

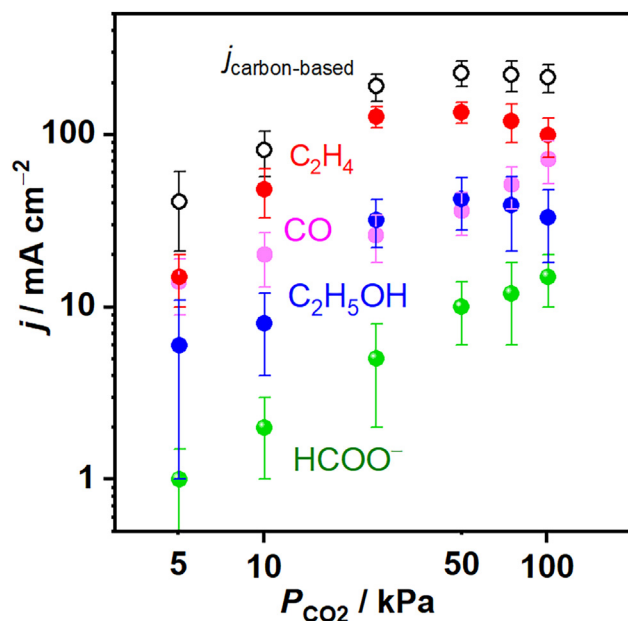


**Figure 4. Pressure-dependent performance in a gas-fed flow cell at 298 K in 0.5 M K<sub>2</sub>SO<sub>4</sub>**

The logarithms of partial current densities of total C-based products, including CO, HCOO<sup>-</sup>, C<sub>2</sub>H<sub>4</sub>, and C<sub>2</sub>H<sub>5</sub>OH, were recorded with respect to the logarithms of the CO<sub>2</sub> partial pressure ranging from 5 to 101 kPa.

consistent with the common RDS of CO and C<sub>2</sub>H<sub>4</sub> formation, consistent with the literature.<sup>11,40</sup>

The reaction rate is directly correlated with the surface coverage of the reactants and/or reaction intermediates on the interface of a catalyst.<sup>41–43</sup> To investigate the effect of  $P_{\text{CO}_2}$  on product distributions, the catalytic performance was examined in a wide range of  $P_{\text{CO}_2}$  spanning from 5 to 101 kPa at 298 K.  $P_{\text{CO}_2}$  was tuned by diluting the feeding gas with Ar, and all the experiments were performed in a 0.5 M K<sub>2</sub>SO<sub>4</sub> electrolyte at  $-1.36$  V<sub>SHE</sub>. Figure 4 displays the reaction rates for each product with respect to  $P_{\text{CO}_2}$  and shows that  $j_{\text{C-based products}}$  increased with increasing  $P_{\text{CO}_2}$  from ca. 50 mA cm<sup>-2</sup> at 5 kPa to 210 mA cm<sup>-2</sup> at 25 kPa, while it stayed almost constant beyond this partial threshold pressure, indicating that CO<sub>2</sub> was not involved in the RDS of CO<sub>2</sub> electroreduction at  $P_{\text{CO}_2} > 25$  kPa. The relationship between the overall  $j_{\text{C-based products}}$  and  $P_{\text{CO}_2}$  was then analyzed for each individual product. More specifically, the  $j_{\text{CO}}$  monotonically increased at higher  $P_{\text{CO}_2}$  and reached the maximum value of 70 mA cm<sup>-2</sup> at 101 kPa; however, the increase was not just a simple linear relationship.  $j_{\text{C}_2\text{H}_4}$  increased from 15 mA cm<sup>-2</sup> at  $P_{\text{CO}_2} = 5$  kPa to 135 mA cm<sup>-2</sup> at  $P_{\text{CO}_2} = 50$  kPa, while it decreased at further increased  $P_{\text{CO}_2}$ , delivering 95 mA cm<sup>-2</sup> at  $P_{\text{CO}_2}$  of 101 kPa.  $j_{\text{C}_2\text{H}_5\text{OH}}$  exhibited a trend similar to that of C<sub>2</sub>H<sub>4</sub>, indicating that the same intermediates existed in early steps. Considering the larger slope of  $j_{\text{CO}}$  between  $P_{\text{CO}_2} = 50$  kPa and  $P_{\text{CO}_2} = 100$  kPa, this shift in the reaction order is probably a consequence of the varied coverage of reactant CO<sub>2</sub> and key intermediate CO. Competition between CO desorption and C–C coupling prevails at all conditions. Increased \*CO<sub>2</sub> might induce perturbation of the binding energy of CO due to adsorbate–adsorbate interactions. Therefore, the suppression of C<sub>2</sub> formation under higher  $P_{\text{CO}_2}$  might originate from enhanced desorption of \*CO due to repulsive interactions with adjacent \*CO<sub>2</sub> adsorbates. It is worth mentioning that the mechanism of enhancement of C<sub>2</sub>H<sub>4</sub> and C<sub>2</sub>H<sub>5</sub>OH formation during CO<sub>2</sub> electroreduction

was significantly different from that during CO electroreduction, where lower  $P_{\text{CO}}$  favored  $\text{C}_2\text{H}_4$  and  $\text{C}_2\text{H}_5\text{OH}$  formation at the expense of acetate and n-PrOH due to the suppression of surface-bound ketene formation and dimerization step between C2 intermediates and adsorbed CO in CO electroreduction.<sup>14</sup>

In addition, the  $j_{\text{HCOO}^-}$  initially increased almost proportionally until it reached a plateau at 75 kPa of  $\text{CO}_2$ , which showed no obvious correlation with others. These findings, together with previous reports, indicated that  $\text{HCOO}^-$  formation deviated from other C-based products in an early step of  $\text{CO}_2$  reduction before the C–C coupling step. Of note,  $j_{\text{H}_2}$  was expected to be suppressed with increasing  $P_{\text{CO}_2}$  (below about 25 kPa), and then it stayed almost constant above this partial threshold pressure (Figure S6). In contrast, there is no transition in the reaction order in addition to  $\text{C}_{2+}$  products on Cu in conventional aqueous cells.<sup>44</sup> Overall, pressure-dependent electrochemical  $\text{CO}_2$  reduction yielded different trends in the conventional aqueous cell and the gas-fed flow cell, most likely resulting from the distinct local reaction environments.<sup>44</sup>

### Temperature-dependent effects on electrochemical $\text{CO}_2$ reduction

The significance of reaction temperature is frequently overlooked in electrochemical  $\text{CO}_2$  reduction. Previous studies mainly focused on electrocatalyst screening at room temperature or even lower temperatures.<sup>6,45,46</sup> It has been reported that lower temperatures suppressed the HER and selectively increased  $\text{CO}_2$  reduction due to higher  $\text{CO}_2$  solubility in electrolytes. However, practical electrolyzers always need to work at increased temperatures to reduce ohmic resistance and kinetic overpotentials. Although some studies have already discussed the impact of temperature on  $\text{CO}_2$  reduction over Cu, this gap between the available and the target hampers the rational development of electrocatalysts and reaction systems.<sup>24,25,47–49</sup> The sensitivity of temperature on electrochemical  $\text{CO}_2$  reduction was carefully investigated at  $P_{\text{CO}_2} = 101$  kPa in a gas-fed flow cell, and the cell temperature was varied from 298 to 353 K. Figure 5A plots the applied potentials and cumulative FEs at a fixed current density ( $400 \text{ mA cm}^{-2}$ ) as a function of the temperature. When the operation temperature increased from 298 to 353 K, the applied potential decreased from ca. 1.45 to ca. 1.37 V versus SHE. Even though the thermodynamic equilibrium potential shifts with temperature, this shift is only less than ca. 15 mV in the investigated temperature range, which indicates that most of the reduction of applied potentials results from the enhanced reaction kinetics. Regarding the product distribution,  $\text{FE}_{\text{H}_2}$  slightly increased at <333 K with elevating temperature, while it increased significantly up to ca. 42%  $\text{FE}_{\text{H}_2}$  at 353 K.  $\text{H}_2$  evolution starts to dominate the surface reactions on Cu GDEs, suggesting that  $\text{CO}_2$  availability seems to be limited at 353 K. Of the C-based products,  $\text{C}_2\text{H}_4$  and liquid products including  $\text{C}_2\text{H}_5\text{OH}$ , n-PrOH, acetate, and  $\text{HCOO}^-$  all exhibited a decreasing trend with increasing temperature. Conversely, the FE of CO was initially 16% at 298 K but increased to ca. 43% at 333 K and remained similar at 353 K. Overall,  $\text{FE}_{\text{CO}}$  with respect to temperature suggests that higher temperature favored CO while reducing  $\text{C}_{2+}$  and  $\text{HCOO}^-$  at <333 K, and the competing  $\text{H}_2$  evolution reaction at 353 K was able to suppress the further increment of  $\text{FE}_{\text{CO}}$ .

To better understand the effects of mass transportation on product distributions at increased temperatures, we modeled the concentration of  $\text{CO}_2$  at the electrode-electrolyte interface (see supplemental information for details).  $\text{CO}_2$  availability in the catalyst layer seems to be sufficient at <333 K, resulting in a relatively lower  $\text{FE}_{\text{H}_2}$ . However, the further decreased  $\text{CO}_2$  concentration at 353 K likely limited the  $\text{CO}_2$  reduction and shifted surface reactions to  $\text{H}_2$  evolution. Moreover, due to the

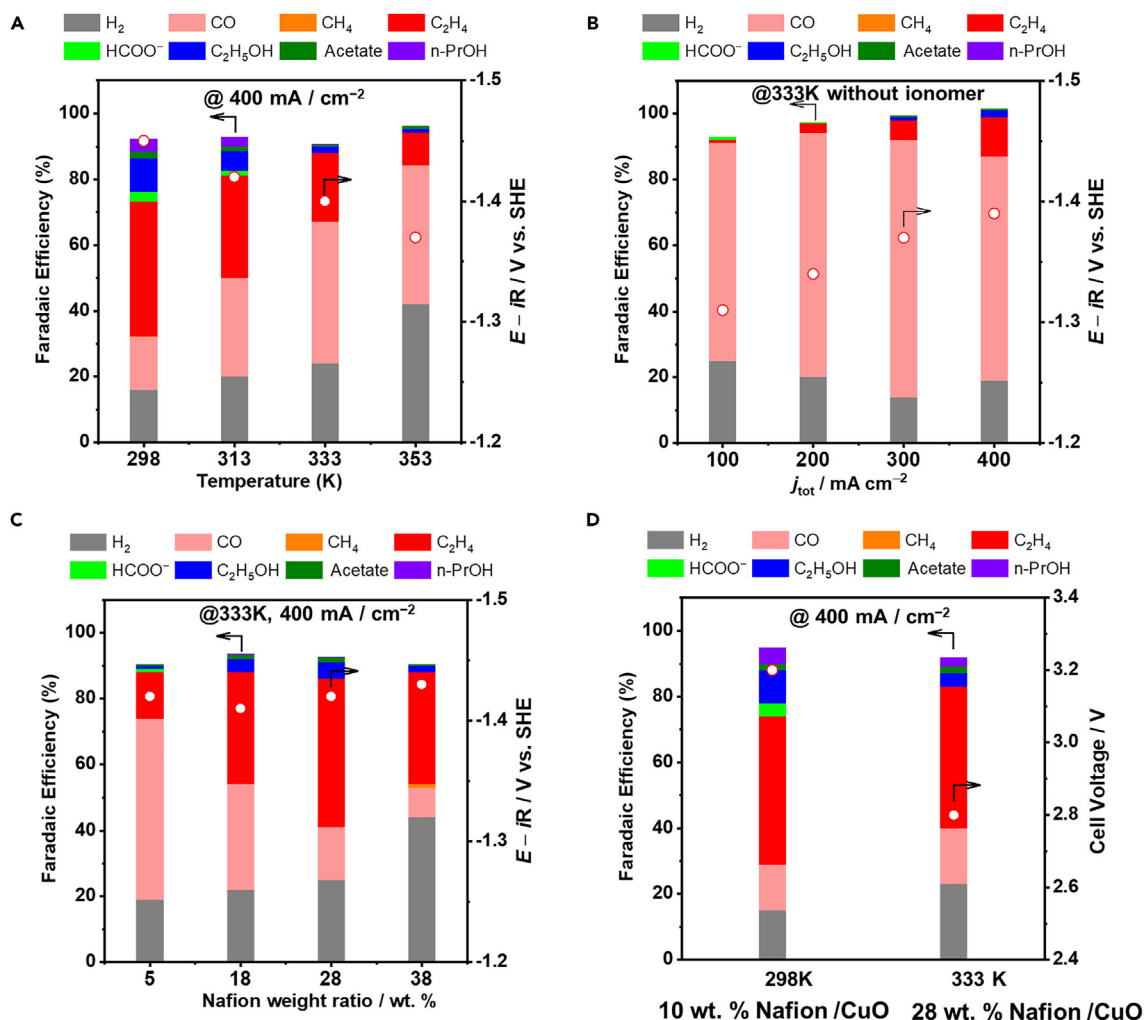


**Figure 5. Temperature-dependent performance of CO<sub>2</sub> electroreduction at 101 kPa CO<sub>2</sub>**

(A) The applied potential and cumulative faradic efficiencies were plotted as a function of temperature at  $-400 \text{ mA cm}^{-2}$  in a gas-fed flow cell. (B) The applied potentials and cumulative faradic efficiencies were recorded versus current densities on a bare Cu GDE at 333 K. (C) The applied potentials and cumulative faradic efficiencies were compiled versus Nafion ionomer content at 333 K and  $400 \text{ mA cm}^{-2}$ . (D) Catalytic performance on 10 wt % Nafion/Cu at 298 K and 28 wt % Nafion/Cu at 333 K in a catholyte-free MEA system.

demonstrated negligible differences in the activation energy of CO desorption between the metal-gas interface and the electrode-electrolyte,<sup>50</sup> the reported CO desorption activation energy ( $10\text{--}20 \text{ kJ mol}^{-1}$ ) can be used to interpret the increased  $FE_{\text{CO}}$  and decreased  $FE_{\text{C}_2\text{H}_4}$  and  $FE_{\text{HCOO}^-}$  resulting from the decreased CO coverage at increased temperature due to the CO thermally excited desorption.<sup>51</sup>

Ionomers with hydrophobic chains are reported to be indispensable at room temperature to construct a gas-electrode-electrolyte interface to increase CO<sub>2</sub> diffusion for high-flux CO<sub>2</sub> electrolysis.<sup>52,53</sup> However, a bare Cu GDE without Nafion ionomer was not examined at high temperatures. Figure 5B presents the dependence of applied potentials and cumulative FEs on current densities over bare Cu at 333 K. Interestingly, CO evolution dominated the surface reaction on bare Cu, and the HER was always suppressed at  $FE_{\text{H}_2} < 25\%$ . The maximum  $FE_{\text{CO}}$  of ca. 80% was achieved at  $j_{\text{tot}} = 300 \text{ mA cm}^{-2}$ , and  $j_{\text{CO}}$  could reach  $280 \text{ mA cm}^{-2}$  at  $-1.39 \text{ V}$  versus SHE. A plausible reaction pathway to exclusively produce CO over a bare Cu surface

was ascribable to the enhanced  $\text{CO}_2$  diffusion coefficient in the surface aqueous layer by a factor of 1.3–1.4 in the catalyst layer and the CO desorption rate on the Cu surface (more discussion in the following section).

We know that local reaction environments, including temperature and  $P_{\text{CO}_2}$ , significantly affected the activity and selectivity of  $\text{CO}_2$  reduction; these relationships point to a scenario in which modulating the diffusion flux of reactants (e.g.,  $\text{CO}_2$  and  $\text{H}_2\text{O}$ ) and key intermediates (e.g., CO) can selectively catalyze  $\text{CO}_2$  to specific products. To further change the local reaction environment, different contents of Nafion ionomer were then introduced into the Cu GDEs. Figure 5C shows the applied potentials and cumulative FEs at  $400 \text{ mA cm}^{-2}$  and 333 K as a function of the ionomer/catalyst weight ratio at a fixed loading of Cu, which displays a strong dependence on ionomer content. Less ionomer content (e.g., 5 wt %) directs  $\text{CO}_2$  reduction toward CO, and increased ionomer (e.g., 18 and 28 wt %) facilitated  $\text{C}_2\text{H}_4$  formation, while overloading of ionomer (e.g., 38 wt %) in Cu GDEs dramatically accelerated  $\text{H}_2$  evolution. After the ionomer/Cu composition was optimized, the maximum  $\text{FE}_{\text{C}_2\text{H}_4}$  increased up to 45% at  $-1.42 \text{ V}$  versus SHE, similar to the as-obtained maximum  $\text{FE}_{\text{C}_2\text{H}_4}$  at 298 K. The enhancement of  $\text{C}_2\text{H}_4$  formation at 333 K likely comes from the reservoir of the key intermediate CO in the Nafion ionomer on the Cu layer.

In contrast, both Cu GDE without ionomer and the optimized Nafion ionomer/Cu GDE (28 wt %) at 298 K delivered an  $\text{FE}_{\text{H}_2}$  of >70% (Figure S7), likely due to the  $\text{CO}_2$  mass transport limitation. To provide deeper insights into the changes in product distributions under varied conditions, the mass transport model was established to reveal the tuned mass transport of the reactants (e.g.,  $\text{CO}_2$  and  $\text{H}_2\text{O}$ ) and key intermediate (e.g., \*CO) on the Cu surface with different microenvironment modifications (see supplemental information for more detail). On the basis of these findings, the optimized electrode (28 wt %) was transferred to the MEA system as a cathodic GDE, where an anion exchange membrane is sandwiched to separate the cathode and the anode ( $\text{IrO}_2/\text{Ti}$  felt) compartments. Compared to that of the best electrode at 298 K, the cell voltage was reduced by up to 15% when the operating temperature was increased from 298 to 333 K at  $400 \text{ mA cm}^{-2}$  (Figure 5D), mainly resulting from both the facilitated electrode reactions and the ionic conduction. Importantly, their product distributions remained nearly constant.

To understand the role of Nafion ionomer at the surface of Cu GDEs on the coverage of CO, we performed CO temperature programmed desorption (Figure 6A). Two CO desorption peaks at approximately 308 and 353 K appeared in the presence of the Nafion ionomer layer, which most likely arose from physically confined CO and chemically bound CO near the catalyst surface.<sup>54,55</sup> In addition, it is interesting to note that the formation rate of  $\text{C}_2\text{H}_4$  during  $\text{CO}_2$  reduction over ionomer (28 wt %)/Cu was superior to that of ionomer (10 wt %)/Cu at 333 K and 101 kPa  $\text{CO}_2$  at  $400 \text{ mA cm}^{-2}$ ; however, the gap between them was increasingly narrowing when introducing CO in the feeding gas, and they almost overlapped at the high CO concentrations (>60%) (Figure 6B). These findings further support our hypothesis regarding the existence of Nafion ionomer in the catalyst layer to increase CO coverage during  $\text{CO}_2$  reduction at 333 K. In parallel, some potential contributions to perturb product distributions at increased temperature cannot be simply excluded, including electrode hydrophobicity, electrolyte surface tension, and dynamic viscosity.<sup>56,57</sup> With rising temperature, the hydrophobicity of the Cu GDE decreased, especially for lower Nafion ionomer content (e.g., 10 wt %). Regarding the surface tension and viscosity of the electrolyte in Figure 6C, the decreasing trends with elevated temperature herein

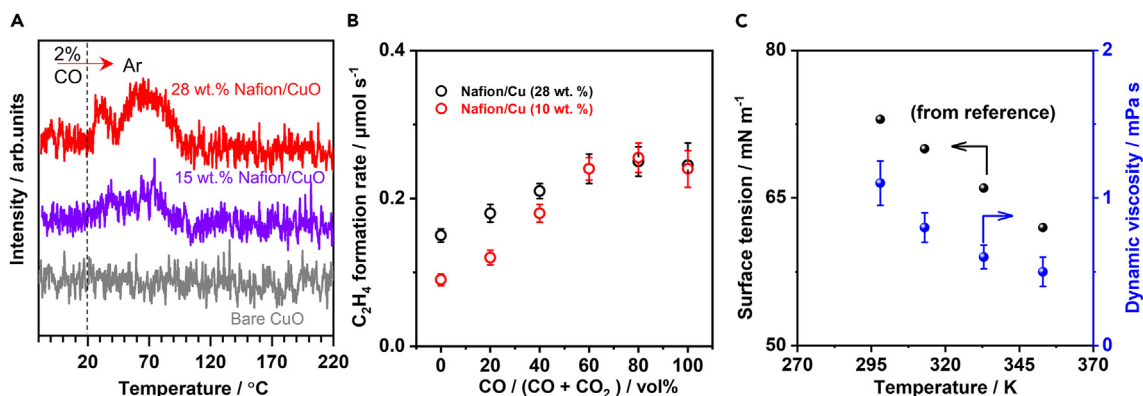


**Figure 6.** Characterization of ionomer decoration of gas-diffusion Cu electrodes

(A) CO temperature programmed desorption of various Nafion/Cu composites.

(B) The reaction rates of  $C_2H_4$  on Nafion/Cu (10 wt %) and Nafion/Cu (28 wt %) at  $400\text{ mA cm}^{-2}$  and  $333\text{ K}$  versus CO partial pressure in  $CO_2$  feeding gas.

(C) The surface tension (from Vargaftik et al.<sup>54</sup>) and dynamic viscosity of electrolyte as a function of temperature.

indicated that operation temperature altered the gas-electrode-electrolyte interface, leading to changes of some key species (e.g.,  $*CO_2$ ,  $H_2O$ , and  $*CO$ ).

Overall, changes in catalyst layer structure with or without the ionomer layer (e.g., chemical composition, thickness, and porosity) affect the mass transport of the reactants (e.g.,  $CO_2$  and  $H_2O$ ) and key intermediate (e.g.,  $CO$ ) during  $CO_2$  reduction, leading to different product distributions at different operating conditions. Please see Figures S8, S9, and S10 for detailed discussions. Moreover, this microenvironment modification by a cation-and-anion-conducting ionomer coating has also been previously observed to tune the  $CO_2/H_2O$  ratio on Cu during  $CO_2$  electroreduction in traditional H-type cells at room temperature.<sup>58</sup> It is important to note that there are other potential factors influencing the rate and selectivity in the presence of an ionomer, such as modulation of adsorption, ion distribution on the surface, or alteration of the electronic structure of the electrocatalyst. These possibilities cannot be easily dismissed. To gain a deeper understanding of the reaction mechanism for  $CO_2$  electroreduction under varying working conditions, further research is required, including *operando* experiments and theoretical calculations, to provide additional evidence and insights.

## DISCUSSION

This study elucidated the impact of the prominent beyond catalyst factors on the performance of  $CO_2$  electroreduction over a Cu GDE at industrially relevant current densities. First, flake-shaped CuO was prepared by hydrothermal synthesis, which selectively electrocatalyzes  $CO_2$  reduction in a gas-fed flow cell, delivering a  $j_{C_2+}$  of ca.  $400\text{ mA cm}^{-2}$  at  $-1.46\text{ V}_{SHE}$  under  $101\text{ kPa } CO_2$  and  $298\text{ K}$ . We have confirmed that the anion identity and buffer capacity of an electrolyte have a negligible impact on  $CO$ ,  $C_2H_4$ ,  $HCOO^-$ , and  $CH_3CH_2OH$ , suggesting that their RDSs do not involve the incorporation of hydrogen atoms. Analyzing the kinetic data as a function of  $P_{CO_2}$  and reaction temperature disclosed that higher  $P_{CO_2}$  ( $>25\text{ kPa}$ ) or higher reaction temperature ( $\leq 333\text{ K}$ ) favored  $CO$  formation at the expense of  $C_{2+}$  products and  $HCOO^-$ , where  $j_{C_2H_4}$  at  $P_{CO_2} = 40\text{ kPa}$  was approximately 1.5 times higher than that at  $P_{CO_2} = 101\text{ kPa}$  at  $298\text{ K}$ ; compared to that examined at  $298\text{ K}$ , a decline in overpotential (ca.  $80\text{ mV}$ ) and increased selectivity of  $CO$  by a factor of ca. 3 at  $333\text{ K}$  and  $400\text{ mA cm}^{-2}$  were observed, suggesting the importance of the beyond

catalyst phenomena. Finally, product distribution control at 333 K was achieved by engineering the structure of Cu GDE, where CO was exclusively produced on bare Cu, and C<sub>2+</sub> was facilitated by introducing optimized Nafion ionomer content into the catalyst layer, likely resulting from the diffusion flux variations of the reactants (e.g., CO<sub>2</sub> and H<sub>2</sub>O) and key intermediate (e.g., CO). Overall, we describe a proven blueprint for local reaction environment optimization for product distribution control at meaningful production rates. MEAs equipped with GDEs at elevated temperatures have shown great potential to overcome the low EE of CO<sub>2</sub> reduction while bringing us close to its practical implementation.

## EXPERIMENTAL PROCEDURES

### Resource availability

#### Lead contact

Requests for further information and resources should be directed to and will be fulfilled by the lead contact, K. Takanebe, at [takanabe@chemsys.t.u-tokyo.ac.jp](mailto:takanabe@chemsys.t.u-tokyo.ac.jp).

#### Materials availability

This study did not generate new materials.

#### Data and code availability

This study did not generate any datasets.

### Materials

The following commercial chemicals were used without further purification. CuCl<sub>2</sub> 2H<sub>2</sub>O (≥99.9%), NaOH (99%), KOH (99.99%), K<sub>2</sub>SO<sub>4</sub> (99%), H<sub>3</sub>PO<sub>4</sub> (ACS reagent), KHCO<sub>3</sub> (≥99.7%), H<sub>2</sub>C<sub>2</sub>O<sub>4</sub> (≥99%), Na<sub>2</sub>CO<sub>3</sub> H<sub>2</sub>O (≥95%), HCl (ACS reagent), urea (ACS reagent), 2-propanol (≥99.5%), dimethyl sulfoxide (DMSO, ≥99.9%), Nafion 117 (5%), and D<sub>2</sub>O (99.9 atom % D) were ordered from Sigma-Aldrich. Ni(NO<sub>3</sub>)<sub>2</sub> 6H<sub>2</sub>O (97.0%), Fe(NO<sub>3</sub>)<sub>3</sub> 9H<sub>2</sub>O (99.0%), and tetrahydrofuran (THF; guaranteed reagent) were purchased from FUJIFILM Wako Pure Chemical. The GDL (Sigracet 39BC) come from the Fuel Cell Store.

### Electrode preparation

#### Cu GDE preparation

CuO synthesis was done following a modified procedure. Fifty milliliters of 1.2 M NaOH aqueous solution was added slowly to 25 mL of 1 M CuCl<sub>2</sub> aqueous solution, and the resultant mixture was stirred for 30 min. Subsequently, the mixture was transferred into a 150-mL Teflon-lined autoclave and heated at 130°C for 18 h. The desired CuO composite was obtained by washing with deionized (DI) water (18.2 MΩ cm) and then vacuum drying. CuO (50 mg) was dispersed in the mixed solvent containing 5 mL 2-propanol/5 mL THF and sonicated for 15 min. Then, a calculated amount of Nafion 117 solution was added to the solution, and the suspension was sonicated for another 15 min. Last, the working electrode was prepared by spray-coating this catalyst ink onto a GDL with dimensions of 3 × 1 cm on 353 K hot plate. The working area was always 1 × 1 cm.

#### Anode electrode preparation

The NiFeO<sub>x</sub>/Ni foam electrode was prepared using hydrothermal synthesis. First, a mixed solution containing 1 mmol of Fe(NO<sub>3</sub>)<sub>3</sub> 9H<sub>2</sub>O, 1 mmol of Ni(NO<sub>3</sub>)<sub>2</sub> 6H<sub>2</sub>O, and 5 mmol of urea was prepared and aged for 30 min. Then, the as-obtained solution was transferred to a 150-mL Teflon-lined autoclave including the acid-treated Ni foam and 80 mL of a mixed solution. The reaction temperature was 120°C and lasted 12 h to get the desired NiFeO<sub>x</sub>/Ni foam electrode. In the MEA, IrO<sub>x</sub>/Ti felt was

prepared by the electrodeposition method as the counter electrode at room temperature. The detailed procedure can be found in our previous study.

### Electrochemical measurements

The catalytic performance was investigated using a three-electrode setup, where the Cu GDE, NiFeOx/Ni foam, and Ag/AgCl (saturated KCl solution) were used as cathode, anode, and reference electrode, respectively. Various electrolytes were circulated in the given catholyte and anolyte reservoirs using a peristaltic pump and a gas-liquid mixed pump, respectively. Gaseous CO<sub>2</sub> (20 mL min<sup>-1</sup> unless otherwise noted) was supplied in a gas chamber and went through the GDL to diffuse into the electrode surface. The whole system was put in an oven to tune the working temperature. The temperature of the electrolyte and reactor was measured using low-noise miniature thermocouples (Omega Engineering).

In addition, the catholyte-free MEA was built with a 1.0-cm<sup>2</sup> serpentine flow field. An anion-exchange membrane (Sustainion 37-50, Dioxide Materials) was utilized to separate the anode and cathode with zero gaps. The temperature-control system was the same as that used in the three-electrode setup. It should be noted that the water trap treated with an ice bath was introduced to capture the evaporated liquid products, mainly including C<sub>2</sub>H<sub>5</sub>OH and n-PrOH. CP and cyclic voltammetry (CV) experiments were performed using a BioLogic potentiostat electrochemical workstation. Each potential was recorded for 30 min to reach a steady state, and three injections were analyzed for gas products. The ohmic resistance was obtained by electrochemical impedance spectroscopy with 85% compensation.

### Product detection

Gaseous products were quantified by an online GC system (Shimadzu GC-2014) equipped with two detectors: a thermal conductivity detector (TCD) with a ShinCarbon column (for H<sub>2</sub> and CO) and a flame ionization detector (FID) with a GS-Gaspro column (for hydrocarbon products). The outlet gas was injected into the GC through an autosampling loop. The partial current density ( $j_i$ ) and FE were calculated using the following Equation 1:

$$FE(i) = \frac{\text{Gas flow rate} \times \text{Concentration of the product}(i)}{\text{Total charge transfer during the electrolysis}/nF} \quad (\text{Equation 1})$$

Liquid production was analyzed using <sup>1</sup>H NMR on a Bruker A VIII 400 MHz NMR spectrometer. The NMR samples were prepared by mixing 500 μL of the collected electrolyte after electrolysis, 100 μL D<sub>2</sub>O, and 50 μL standard solution containing 2.38 mM DMSO and 10 mM phenol:

$$FE = \frac{\text{Catholyte volume} \times \text{Concentration of the product}(i)}{\text{Total charge transfer during the electrolysis}/nF} \quad (\text{Equation 2})$$

In this study, the gas flow rate was 20 mL min<sup>-1</sup>, the concentration of the product ( $i$ ) was calculated based on GC peak area, the faradic constant  $F = 9.65 \times 10^4$  A s mol<sup>-1</sup>, and  $n$  is the number of electron transfers, where  $n$  is 2 for CO and HCOO<sup>-</sup>, 12 for both C<sub>2</sub>H<sub>4</sub> and C<sub>2</sub>H<sub>5</sub>OH, 18 for n-PrOH, and 8 for acetate generation.

### Material characterization

The morphologies of working electrodes were characterized by SEM (JSM-IT800, JEOL), and the acceleration voltage was 1 kV. TEM images were obtained using a JEM 2100 F (200 kV). The surface chemical states of the Cu-based composite were characterized by XPS (JPS-9010MC, JEOL) using Mg K $\alpha$  radiation. The water contact angle was collected by a high-speed camera and a long-working-distance lens (VW-600M and

VH-250L, Keyence). The X-ray patterns were collected using a Rigaku MiniFlex. Diffuse reflectance infrared Fourier transform spectroscopy was obtained using a JASCO FT/IR-4600 equipped with a mercury cadmium telluride (MCT) detector at the liquid nitrogen temperature and a diffuse-reflectance infrared cell with a KBr window.

### Raman experiments

The *in situ* surface-enhanced Raman spectroscopy was carried out using an inverted confocal Raman microscope (JASCO RMP-510) equipped with an He/Ne laser (532 nm). A homemade glass cell was used in this study, and the temperature of the electrolyte was controlled by a hot plate. A platinum mesh and Ag/AgCl (saturated KCl solution) were utilized as counter and reference electrode, respectively. Chronoamperometry was performed for 20 min at each applied potential to collect the spectroscopy.

### CO temperature programmed desorption

The temperature programmed desorption experiments were carried out in a U-shaped flow system connected to a Q-mass spectrometer (Inficon Transpector CPM). Nafion ionomer/CuO was loaded in the glass tube reactor. CO (2%, 20 mL min<sup>-1</sup>) was supplied at 293 K and left for 30 min. Next, the gas was switched to Ar flow (20 mL min<sup>-1</sup>), and then the sample was heated to 473 K. Mass signal *m/z* = 28 was used to qualitatively measure the CO.

### SUPPLEMENTAL INFORMATION

Supplemental information can be found online at <https://doi.org/10.1016/j.checat.2024.101030>.

### ACKNOWLEDGMENTS

A part of this work was supported by JSPS KAKENHI grant no. 19KK0126 and Asahi Kasei Corporation collaborative funding.

### AUTHOR CONTRIBUTIONS

K.T. supervised the project. X.L. and K.T. conceived the idea and designed the experiments. X.L. and T.G. performed all the performance tests and characterizations. Y.Y. helped do the simulation study. All authors contributed to the data analysis and writing of the manuscript.

### DECLARATION OF INTERESTS

The authors declare no competing interests.

Received: February 21, 2024

Revised: April 21, 2024

Accepted: May 22, 2024

Published: June 17, 2024

### REFERENCES

- Stephens, I.E., Chan, K., Bagger, A., Boettcher, S.W., Bonin, J., Boutin, E., Buckley, A.K., Buonsanti, R., Cave, E.R., and Chang, X. (2022). 2022 roadmap on low temperature electrochemical CO<sub>2</sub> reduction. *JPhys Energy* 4, 042003.
- De Luna, P., Hahn, C., Higgins, D., Jaffer, S.A., Jaramillo, T.F., and Sargent, E.H. (2019). What would it take for renewably powered electrosynthesis to displace petrochemical processes? *Science* 364, eaav3506.
- Overa, S., Feric, T.G., Park, A.-H.A., and Jiao, F. (2021). Tandem and hybrid processes for carbon dioxide utilization. *Joule* 5, 8–13.
- O'Brien, C.P., Miao, R.K., Liu, S.J., Xu, Y., Lee, G., Robb, A., Huang, J.E., Xie, K., Bertens, K., Gabardo, C.M., et al. (2021). Single Pass CO<sub>2</sub> Conversion Exceeding 85% in the Electrosynthesis of Multicarbon Products via Local CO<sub>2</sub> Regeneration. *ACS Energy Lett.* 6, 2952–2959.
- Huang, J.E., Li, F., Ozden, A., Sedighian Rasouli, A., Garcia de Arquer, F.P., Liu, S., Zhang, S., Luo, M., Wang, X., Lum, Y., et al. (2021). CO<sub>2</sub> electrolysis to multicarbon

- products in strong acid. *Science* **372**, 1074–1078.
- Nitopi, S., Bertheussen, E., Scott, S.B., Liu, X., Engstfeld, A.K., Horch, S., Seger, B., Stephens, I.E.L., Chan, K., Hahn, C., et al. (2019). Progress and Perspectives of Electrochemical CO<sub>2</sub> Reduction on Copper in Aqueous Electrolyte. *Chem. Rev.* **119**, 7610–7672.
  - Birdja, Y.Y., Pérez-Gallent, E., Figueiredo, M.C., Göttle, A.J., Calle-Vallejo, F., and Koper, M.T.M. (2019). Advances and challenges in understanding the electrocatalytic conversion of carbon dioxide to fuels. *Nat. Energy* **4**, 732–745.
  - Shin, H., Hansen, K.U., and Jiao, F. (2021). Techno-economic assessment of low-temperature carbon dioxide electrolysis. *Nat. Sustain.* **4**, 911–919.
  - Alerte, T., Edwards, J.P., Gabardo, C.M., O'Brien, C.P., Gaona, A., Wicks, J., Obradović, A., Sarkar, A., Jaffer, S.A., MacLean, H.L., et al. (2021). Downstream of the CO<sub>2</sub> Electrolyzer: Assessing the Energy Intensity of Product Separation. *ACS Energy Lett.* **6**, 4405–4412.
  - Burdyn, T., and Smith, W.A. (2019). CO<sub>2</sub> reduction on gas-diffusion electrodes and why catalytic performance must be assessed at commercially-relevant conditions. *Energy Environ. Sci.* **12**, 1442–1453.
  - Lu, X., Dereli, B., Shinagawa, T., Eddaoudi, M., Cavallo, L., and Takanabe, K. (2022). High current density microkinetic and electronic structure analysis of CO<sub>2</sub> reduction using Co and Fe complexes on gas diffusion electrode. *Chem Catal.* **2**, 1143–1162.
  - Lu, X., Ahsaine, H.A., Dereli, B., Garcia-Esparza, A.T., Reinhard, M., Shinagawa, T., Li, D., Adil, K., Tchalala, M.R., Kroll, T., et al. (2021). Operando Elucidation on the Working State of Immobilized Fluorinated Iron Porphyrin for Selective Aqueous Electroreduction of CO<sub>2</sub> to CO. *ACS Catal.* **11**, 6499–6509.
  - Resasco, J., and Bell, A.T. (2020). Electrocatalytic CO<sub>2</sub> reduction to fuels: progress and opportunities. *Trends in Chemistry* **2**, 825–836.
  - Lu, X., Shinagawa, T., and Takanabe, K. (2023). Product Distribution Control Guided by a Microkinetic Analysis for CO Reduction at High-Flux Electrocatalysis Using Gas-Diffusion Cu Electrodes. *ACS Catal.* **13**, 1791–1803.
  - Clark, E.L., Resasco, J., Landers, A., Lin, J., Chung, L.-T., Walton, A., Hahn, C., Jaramillo, T.F., and Bell, A.T. (2018). Standards and Protocols for Data Acquisition and Reporting for Studies of the Electrochemical Reduction of Carbon Dioxide. *ACS Catal.* **8**, 6560–6570.
  - Christensen, O., Zhao, S., Sun, Z., Bagger, A., Lauritsen, J.V., Pedersen, S.U., Daasbjerg, K., and Rossmeisl, J. (2022). Can the CO<sub>2</sub> Reduction Reaction Be Improved on Cu: Selectivity and Intrinsic Activity of Functionalized Cu Surfaces. *ACS Catal.* **12**, 15737–15749.
  - Jouny, M., Luc, W., and Jiao, F. (2018). High-rate electroreduction of carbon monoxide to multi-carbon products. *Nat. Catal.* **1**, 748–755.
  - Marcandalli, G., Villalba, M., and Koper, M.T.M. (2021). The Importance of Acid-Base Equilibria in Bicarbonate Electrolytes for CO<sub>2</sub> Electrochemical Reduction and CO Reoxidation Studied on Au(hkl) Electrodes. *Langmuir* **37**, 5707–5716.
  - Banerjee, R., Ge, N., Han, C., Lee, J., George, M.G., Liu, H., Muirhead, D., Shrestha, P., and Bazylak, A. (2018). Identifying in operando changes in membrane hydration in polymer electrolyte membrane fuel cells using synchrotron X-ray radiography. *Int. J. Hydrogen Energy* **43**, 9757–9769.
  - Karatza, D., Konstantopoulos, C., Chianese, S., Diplas, S., Svec, P., Hristoforou, E., and Musmarra, D. (2021). Hydrogen production through water splitting at low temperature over Fe<sub>3</sub>O<sub>4</sub> pellet: Effects of electric power, magnetic field, and temperature. *Fuel Process. Technol.* **211**, 106606.
  - Yin, Z., Peng, H., Wei, X., Zhou, H., Gong, J., Huai, M., Xiao, L., Wang, G., Lu, J., and Zhuang, L. (2019). An alkaline polymer electrolyte CO<sub>2</sub> electrolyzer operated with pure water. *Energy Environ. Sci.* **12**, 2455–2462.
  - Löwe, A., Rieg, C., Hierlemann, T., Salas, N., Kopljar, D., Wagner, N., and Klemm, E. (2019). Influence of Temperature on the Performance of Gas Diffusion Electrodes in the CO<sub>2</sub> Reduction Reaction. *Chemelectrochem* **6**, 4497–4506.
  - Hori, Y., Takahashi, I., Koga, O., and Hoshi, N. (2002). Selective formation of C<sub>2</sub> compounds from electrochemical reduction of CO<sub>2</sub> at a series of copper single crystal electrodes. *J. Phys. Chem. B* **106**, 15–17.
  - Ahn, S.T., Abu-Baker, I., and Palmore, G.R. (2017). Electroreduction of CO<sub>2</sub> on polycrystalline copper: Effect of temperature on product selectivity. *Catal. Today* **288**, 24–29.
  - Vos, R.E., Kolmeijer, K.E., Jacobs, T.S., van der Stam, W., Weckhuysen, B.M., and Koper, M.T.M. (2023). How Temperature Affects the Selectivity of the Electrochemical CO<sub>2</sub> Reduction on Copper. *ACS Catal.* **13**, 8080–8091.
  - Xu, J.F., Ji, W., Shen, Z.X., Li, W.S., Tang, S.H., Ye, X.R., Jia, D.Z., and Xin, X.Q. (1999). Raman spectra of CuO nanocrystals. *J. Raman Spectrosc.* **30**, 413–415.
  - Song, X., Xu, L., Sun, X., and Han, B. (2023). In situ/operando characterization techniques for electrochemical CO<sub>2</sub> reduction. *Sci. China Chem.* **66**, 315–323.
  - Monteiro, M.C.O., Dattila, F., López, N., and Koper, M.T.M. (2022). The Role of Cation Acidity on the Competition between Hydrogen Evolution and CO<sub>2</sub> Reduction on Gold Electrodes. *J. Am. Chem. Soc.* **144**, 1589–1602.
  - Monteiro, M.C.O., Dattila, F., Hagedoorn, B., García-Muelas, R., López, N., and Koper, M.T.M. (2021). Absence of CO<sub>2</sub> electroreduction on copper, gold and silver electrodes without metal cations in solution. *Nat. Catal.* **4**, 654–662.
  - Malkani, A.S., Li, J., Oliveira, N.J., He, M., Chang, X., Xu, B., and Lu, Q. (2020). Understanding the electric and nonelectric field components of the cation effect on the electrochemical CO reduction reaction. *Sci. Adv.* **6**, eabd2569.
  - Ryu, J., Wuttig, A., and Surendranath, Y. (2018). Quantification of Interfacial pH Variation at Molecular Length Scales Using a Concurrent Non-Faradaic Reaction. *Angew. Chem. Int. Ed.* **57**, 9300–9304.
  - Bagger, A., Ju, W., Varela, A.S., Strasser, P., and Rossmeisl, J. (2017). Electrochemical CO<sub>2</sub> reduction: a classification problem. *ChemPhysChem* **18**, 3266–3273.
  - Hammouche, M., Lexa, D., Momenteau, M., and Saveant, J.M. (1991). Chemical catalysis of electrochemical reactions. Homogeneous catalysis of the electrochemical reduction of carbon dioxide by iron(0) porphyrins. Role of the addition of magnesium cations. *J. Am. Chem. Soc.* **113**, 8455–8466.
  - Ringe, S., Clark, E.L., Resasco, J., Walton, A., Seger, B., Bell, A.T., and Chan, K. (2019). Understanding cation effects in electrochemical CO<sub>2</sub> reduction. *Energy Environ. Sci.* **12**, 3001–3014.
  - Resasco, J., Lum, Y., Clark, E., Zeledon, J.Z., and Bell, A.T. (2018). Effects of anion identity and concentration on electrochemical reduction of CO<sub>2</sub>. *Chemelectrochem* **5**, 1064–1072.
  - Hochfilzer, D., Xu, A., Sørensen, J.E., Needham, J.L., Krempl, K., Toudahl, K.K., Kastlunger, G., Chorkendorff, I., Chan, K., and Kibsgaard, J. (2022). Transients in Electrochemical CO Reduction Explained by Mass Transport of Buffers. *ACS Catal.* **12**, 5155–5161.
  - Lv, J.J., Jouny, M., Luc, W., Zhu, W., Zhu, J.J., and Jiao, F. (2018). A highly porous copper electrocatalyst for carbon dioxide reduction. *Adv. Mater.* **30**, 1803111.
  - Shinagawa, T., Obata, K., and Takanabe, K. (2019). Switching of Kinetically Relevant Reactants for the Aqueous Cathodic Process Determined by Mass-transport Coupled with Protolysis. *ChemCatChem* **11**, 5961–5968.
  - Dinh, C.-T., Burdyn, T., Kibria, M.G., Seifitokaldani, A., Gabardo, C.M., Garcia de Arquer, F.P., Kiani, A., Edwards, J.P., De Luna, P., Bushuyev, O.S., et al. (2018). CO<sub>2</sub> electroreduction to ethylene via hydroxide-mediated copper catalysis at an abrupt interface. *Science* **360**, 783–787.
  - Shinagawa, T., Garcia-Esparza, A.T., and Takanabe, K. (2015). Insight on Tafel slopes from a microkinetic analysis of aqueous electrocatalysis for energy conversion. *Sci. Rep.* **5**, 13801.
  - Luo, W., Nie, X., Janik, M.J., and Asthagiri, A. (2016). Facet Dependence of CO<sub>2</sub> Reduction Paths on Cu Electrodes. *ACS Catal.* **6**, 219–229.
  - Lausche, A.C., Medford, A.J., Khan, T.S., Xu, Y., Bligaard, T., Abild-Pedersen, F., Nørskov, J.K., and Studt, F. (2013). On the effect of coverage-dependent adsorbate-adsorbate interactions for CO methanation on transition metal surfaces. *J. Catal.* **307**, 275–282.
  - Cheng, T., Xiao, H., and Goddard, W.A. (2017). Full atomistic reaction mechanism with kinetics for CO reduction on Cu(100) from ab initio molecular dynamics free-energy calculations at

- 298 K. *Proc. Natl. Acad. Sci. USA* **114**, 1795–1800.
44. Wang, L., Nitopi, S.A., Bertheussen, E., Orazov, M., Morales-Guio, C.G., Liu, X., Higgins, D.C., Chan, K., Nørskov, J.K., Hahn, C., and Jaramillo, T.F. (2018). Electrochemical Carbon Monoxide Reduction on Polycrystalline Copper: Effects of Potential, Pressure, and pH on Selectivity toward Multicarbon and Oxygenated Products. *ACS Catal.* **8**, 7445–7454.
  45. Azuma, M., Hashimoto, K., Hiramoto, M., Watanabe, M., and Sakata, T. (1990). Electrochemical Reduction of Carbon Dioxide on Various Metal Electrodes in Low-Temperature Aqueous KHCO<sub>3</sub> Media. *J. Electrochem. Soc.* **137**, 1772–1778.
  46. Mizuno, T., Ohta, K., Kawamoto, M., and Saji, A. (1997). Electrochemical reduction of CO<sub>2</sub> on Cu in 0.1 M KOH-methanol. *Energy Sources* **19**, 249–257.
  47. Vos, R.E., and Koper, M.T.M. (2022). The Effect of Temperature on the Cation-Promoted Electrochemical CO<sub>2</sub> Reduction on Gold. *Chemelectrochem* **9**, e202200239.
  48. Resasco, J., Abild-Pedersen, F., Hahn, C., Bao, Z., Koper, M.T.M., and Jaramillo, T.F. (2022). Enhancing the connection between computation and experiments in electrocatalysis. *Nat. Catal.* **5**, 374–381.
  49. Zong, Y., Chakthranont, P., and Suntivich, J. (2020). Temperature Effect of CO<sub>2</sub> Reduction Electrocatalysis on Copper: Potential Dependency of Activation Energy. *Journal of Electrochemical Energy Conversion and Storage* **17**, 041007.
  50. Geng, B., Cai, J., Liang, S., Liu, S.X., Li, M.F., and Chen, Y.-X. (2010). Temperature effects on CO adsorption/desorption at Pt film electrodes: an electrochemical in situ infrared spectroscopic study. *Phys. Chem. Chem. Phys.* **12**, 10888–10895.
  51. Sandoval, M.J., and Bell, A.T. (1993). Temperature-Programmed Desorption Studies of the Interactions of H<sub>2</sub>, CO, and CO<sub>2</sub> with Cu/SiO<sub>2</sub>. *J. Catal.* **144**, 227–237.
  52. Ding, P., An, H., Zellner, P., Guan, T., Gao, J., Müller-Buschbaum, P., Weckhuysen, B.M., van der Stam, W., and Sharp, I.D. (2023). Elucidating the Roles of Nafion/Solvent Formulations in Copper-Catalyzed CO<sub>2</sub> Electrolysis. *ACS Catal.* **13**, 5336–5347.
  53. García de Arquer, F.P., Dinh, C.-T., Ozden, A., Wicks, J., McCallum, C., Kirmani, A.R., Nam, D.-H., Gabardo, C., Seifitokaldani, A., Wang, X., et al. (2020). CO<sub>2</sub> electrolysis to multicarbon products at activities greater than 1 A cm<sup>-2</sup>. *Science* **367**, 661–666.
  54. Chang, X., Vijay, S., Zhao, Y., Oliveira, N.J., Chan, K., and Xu, B. (2022). Understanding the complementarities of surface-enhanced infrared and Raman spectroscopies in CO adsorption and electrochemical reduction. *Nat. Commun.* **13**, 2656.
  55. Gao, J., Zhang, H., Guo, X., Luo, J., Zakeeruddin, S.M., Ren, D., and Grätzel, M. (2019). Selective C–C Coupling in Carbon Dioxide Electroreduction via Efficient Spillover of Intermediates As Supported by Operando Raman Spectroscopy. *J. Am. Chem. Soc.* **141**, 18704–18714.
  56. Vargaftik, N.B., Volkov, B.N., and Voljak, L.D. (1983). International tables of the surface tension of water. *J. Phys. Chem. Ref. Data* **12**, 817–820.
  57. Kestin, J., Sokolov, M., and Wakeham, W.A. (1978). Viscosity of liquid water in the range – 8 C to 150 C. *J. Phys. Chem. Ref. Data* **7**, 941–948.
  58. Kim, C., Bui, J.C., Luo, X., Cooper, J.K., Kusoglu, A., Weber, A.Z., and Bell, A.T. (2021). Tailored catalyst microenvironments for CO<sub>2</sub> electroreduction to multicarbon products on copper using bilayer ionomer coatings. *Nat. Energy* **6**, 1026–1034.